MASSIVELY-PARALLEL SPECTRAL ELEMENT LARGE EDDY SIMULATION OF A TURBULENT CHANNEL USING WALL MODELS

A Thesis

by

JOSHUA IAN RABAU

Submitted to the Office of Graduate Studies of
Texas A&M University
in partial fulfillment of the requirements for the degree of

MASTER OF SCIENCE

Approved by:

Chair of Committee,	Andrew Duggleby
Committee Members,	Je-Chin Han
	Jean-Luc Guermond
Head of Department,	Andreas A. Polycarpou

May 2013

Major Subject: Mechanical Engineering

ABSTRACT

Wall-bounded turbulent flows are prevalent in engineering and industrial applications. Walls greatly affect turbulent characteristics in many ways including production and propagation of turbulent stresses. While computational fluid dynamics can be used as an important design tool, its use is hindered due to the fine-mesh requirements in the near-wall region to capture all of the pertinent turbulent data. To resolve all relevant scales of motion, the number of grid points scales with Reynolds number as $N \approx \mathrm{Re}^{9/4}$, making it nearly impossible to solve real engineering problems, most of which feature high Reynolds numbers.

A method to help alleviate the resolution requirements is the use of wall models. This method allows for a coarser mesh to be used in which the near-wall region is modeled and the first grid point is placed in the log-law region. The shear stress at the wall is correlated with the velocity at a point outside the near-wall region, drastically reducing the number of elements required and reducing the computational time and cost of the simulation.

The goal of this study was to test the speed increase and element reduction capabilities of combining a wall function solution with the massively-parallel, spectral element solver, Nek5000, and verify the method using a turbulent channel simulation. The first grid point is placed at $y^+ = 100$, in the log-law region, for $Re_\tau = 950$ and the sub-grid scales are modeled using a dynamic Smagorinski model. The results are then compared to a DNS performed by Jiménez and Hoyas for model verification.

DEDICATION

To my parents and sister; Mark, Sharon, and Sabrina Rabau

ACKNOWLEDGEMENTS

I would first like to thank my advisor, Andrew Duggleby, and my professor, Yuval Doron. I have learned so much from both of you in aspects of academia, industry, and life. Graduate school would have been far more difficult to get through without the opportunities and support you have given me, and I look forward to applying all the knowledge that I have acquired toward great things. I would like to thank my lab mate, Joshua Camp, for all of his guidance, help, and advice. You constantly fielded questions and were an enormous resource. I would like to thank the Texas A&M for providing the supercomputing resources granted to me in order to complete my simulations. I would like to thank my very close friends Mark Ballou and Andrew Leavitt for always being there to talk to and get me through the times when graduate school and moving to Texas were hardest, you guys are the best. Finally, I would like to thank my parents, Mark and Sharon, and my sister Sabrina for making me who I am today. Your constant and overwhelming support in all that I do has given me the strength and ability to push forward and succeed. I owe you guys everything and nobody could ask for a better family. I love you all.

NOMENCLATURE

CFD	Computational Fluid Dynamics
DNS	Direct Numerical Simulation
RANS	Reynolds Averaged Navier-Stokes
LES	Large Eddy Simulation
FEM	Finite Element Method
SEM	Spectral Element Method
SGS	Sub-Grid Scale
TLM	Two Layer Method
Re	Reynolds Number
Re_τ	Friction Reynolds Number
U_∞	Characteristic Velocity
GLL	Gauss-Lobatto-Legendre
C_s	Smagorinski Coefficient
y^+	Wall Units in the Wall Normal Direction

Δx^+	Grid Spacing in Streamwise Direction
Δy^+	Grid Spacing in Wall Normal Direction
Δz^+	Grid Spacing in Spanwise Direction
u_τ	Friction Velocity
τ_w	Wall Shear Stress
ρ	Density
ν	Kinematic Viscosity
u_i	Velocity Component
τ_{ij}	SGS Stress Tensor
P	Pressure
μ	Dynamic Viscosity
G	Filter Function
$\bar{S}_{ij}$	Strain Rate Tensor on Filtered Velocity
ν_T	Eddy Viscosity
Δ	Filter Width

ℓ_s Smagorinski Length Scale

δ_{ij} Kronecker Delta

ϕ_n Interpolation Polynomial

L_n Legendre Polynomial

TABLE OF CONTENTS

LIST OF FIGURES

FIGURE Page

LIST OF TABLES

TABLE Page

1 INTRODUCTION

Engineering design is a key aspect in the creation of any product used today. In order for a product to be manufactured, built, and sold, it must first go through a design process. This process is made up of many steps including the two key steps of the detailed design and prototyping and testing. The detailed design is where the product is visualized using solid computer modeling and drawings. From these drawings and computer models, the product is manufactured and assembled in the form of a prototype and thoroughly tested. This is typically an iterative process that requires building many prototypes, performing countless tests, and optimizing the design model. For large, complex products such as airplanes, cars, and gas turbines, this process can quickly become very expensive. When studying and optimizing something such as a gas turbine, engineers are interested in efficiency and losses, among other things. To improve efficiency and limit losses, engineers must understand the behavior of the overall flow and what effects the flow structures and characteristics associated with the system have on its performance and durability. One of the most important flow characteristics to understand is the effect of turbulent flow. Fluid turbulence is a feature of fluid flows, not of specific fluids themselves, that can be advantageous or detrimental depending on the system in question. However, today it is still considered to be one of the unsolved questions of classical physics. Sir Horace Lamb, an influential researcher in the field of fluid mechanics said,

"I am an old man now, and when I die and go to Heaven there are two matters on which I hope for enlightenment. One is quantum electrodynamics and the other is the turbulent motion of fluids. And about the former I am rather more optimistic."

[6]

1.1 Overview of Fluid Turbulence

Although fluid turbulence is unsolved, understanding it and its effects are very important in engineering design. For example, turbulent flow can be both advantageous and detrimental in the study of combustion and power generation. By increasing fluid turbulence in an engine, mixing capabilities of fuel and oxygen are enhanced, leading to more efficient combustion. Conversely, increased fluid turbulence around or near the walls of an engine increase heat transfer capabilities leading to material failure. Turbulent flow also has detrimental effects on external flows, such as around a car or an airplane. Fluid turbulence increases friction drag, thus effecting fuel consumption. By eliminating turbulent flow on up to 40% of the surfaces of an aircraft, the friction drag, which accounts for more than half the total drag of an aircraft, can be reduced up to 16% [26]. By understanding and potentially controlling or managing where and how fluid turbulence occurs, more advanced and efficient designs can be created.

A turbulent flow will transition from laminar flow due to instabilities arising and propagating through the flow and is identified through physical characteristics. Three fundamental characteristics of turbulent flow are increased mixing, increased vorticity, and chaos, or chaotic flow. Turbulent flows are diffusive in nature, causing enhanced rates of heat, mass, and momentum transfer as well as rapid mixing. In laminar flows, mixing occurs naturally due to molecular diffusion (viscosity), however, these effects are seen on much larger scales when the flow becomes turbulent. Fluid turbulence exponentially stretches the interface surface area of fluid particles over which molecular diffusion acts, increasing the speed of mixing. This is important to engineers, who are concerned with drag and heat transfer effects in a system. The second characteristic of a turbulent flow is vorticity. Turbulent flows are rotational,

containing three dimensional vorticies that are generated by the instabilities in the flow or with help from the presence of a wall or an object in the flow. Vortex stretching is a fundamental mechanism that, due to conservation of angular momentum, causes vorticies to lengthen in one direction and thin in another. Larger structures to break into smaller structures, establishing an energy cascade turbulent energy carrying structures or motions, until the kinetic energy is overcome by the viscosity of the fluid. These fluid motions, called eddies, are characterized by a range of length scales, as show in Figure 1.1. The largest, higher energy scales are determined by the size of the geometry, a characteristic length, while the smallest, lower energy scales determined by the Reynolds number.

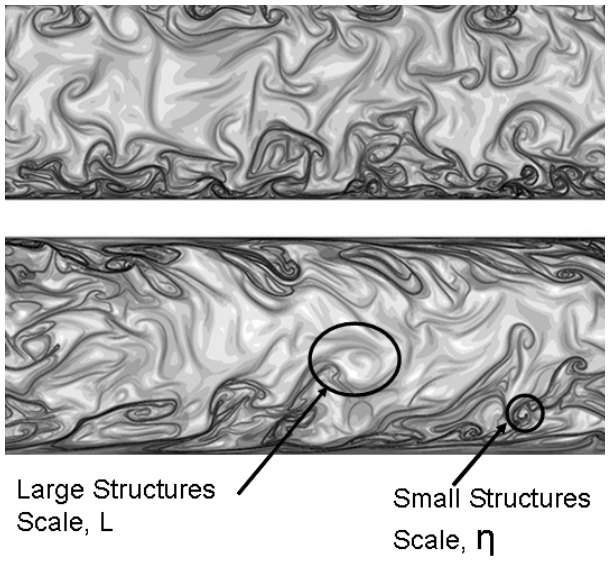

Figure 1.1: Turbulent channel structures. Visualization by Department of Mechanical and Aerospace Engineering at Princeton [12]

Reynolds number is a non-dimensional number defined by characteristic velocity, U_∞, a characteristic length, L, and viscosity, ν. It is essentially a ratio of the inertial

forces to viscous forces.

$$Re = \frac{U_\infty L}{\nu} \tag{1.1}$$

As Reynolds number increases, the range of length scales increases. Turbulent flows are also chaotic. Three important consequences arise from this fact. The first is that turbulent motions are highly irregular. The second is that turbulent flows are sensitive to initial conditions, meaning that the slightest difference in the nature of instabilities in the flow will change the structure of the turbulent flow completely. The third consequence is that turbulent flows are deterministic, meaning equations can be solved for instantaneous flow quantities. However, because of the sensitivity to initial conditions and irregular nature of turbulent flows, it is impractical to solve these equations because describing the turbulent motion as a function of time and space becomes unmanageable. Engineers instead treat the problems statistically instead of deterministically, concerning themselves with statistical averages of turbulent flows such as the average drag over a wing or the average pressure loss, in an attempt to understand what its effects are on systems of interest.

1.2 Background of Techniques

Comprehension of fluid flows are necessary for many fields, industries, and virtually all areas of engineering, specifically understanding the dynamics of turbulent eddies within a flow. However, there is still a large amount of information and many phenomena that are not fully understood. Once theory has been exhausted, knowledge about the system in question can be gained by means of two different paths, experimentation and numerical simulations.

Experimentation is a physical process in which a full prototype, or typically a

scaled model, is created and tests are performed in order to measure the flow physics directly. Experiments may require elaborate setups or special environments such as wind tunnels in order to properly mimic the system of study. Additionally, proper measuring devices are necessary to gather the data needed to study the flow dynamics. A common example of an experiment is placing scaled model of an airfoil or car in a wind tunnel and measuring pressure and velocity data while accelerated air passes over the model, simulating real conditions. Using acquired data, important design quantities, such as drag, can be calculated. Data from experiments can also be used to verify theory and tune mathematical models. (For different experimental measuring techniques, a good source is Goldstein [10]). Real data acquisition is limited to the scope of the measurement devices. It is very difficult to capture certain aspects of the flow physics as well as data for an entire flow field. Experiments are limited to points of interest in which to focus the measurements. Experiments can also be very large, expensive, and require a lot of time to construct the experimental apparatus.

The second method of gaining understanding of a system is through numerical simulations. A set of equations called the Navier-Stokes equations represent the conservation of momentum in a fluid system. Coupled with the continuity equation, conservation of mass, these equations govern the physics of a fluid system. Because these four equations are coupled, non-linear, partial differential equations, an analytical solution is rare or sometimes non-existent without severe assumptions and simple cases. Since the majority of real life flows are more complex than these assumptions will allow, the equations must be solved numerically. Numerical analysis transforms the Navier-Stokes equations from a set of differential equations to discrete difference equations able to be solved numerically, through a process called discretization. While using numerical simulations allows the user to have data at every point within

the domain, validating the data and scheme to ensure accuracy of the method is essential. Validation against experimental data is critical to prove that a numerical method is accurate and can be used to predict real data. Boundary conditions, grid resolution (how the domain is broken down and the size of each element), and the size of the time step taken in advancing the simulation all play a crucial role in the stability and accuracy of a numerical scheme.

1.2.1 Computational Fluid Dynamics

The study of using numerical simulations in order to solve a fluid system is typically referred to as computational fluid dynamics, or CFD for short. CFD is broken down into three different types of simulations, Direct Numerical Simulations (DNS), Reynolds-Averaged Navier-Stokes (RANS), and Large Eddy Simulation (LES). Each method comes with its own strengths and weaknesses, and while they all solve the Navier-Stokes equations, the major difference lies in how the phenomenon of fluid turbulence is dealt with and how the different length scales are solved or modeled, as shown in Figure 1.2.

DNS solves the Navier-Stokes equations directly to determine the instantaneous velocity field without the use of any turbulence modeling. While DNS is conceptually the most basic approach as well as being widely considered the most accurate type of simulation, it comes with a big cost [24]. In order to resolve all of the necessary length scales and time scales, the grid resolution of the domain must be small enough to capture them. The number of grid points needed to perform a three-dimensional DNS scales like $N \sim Re^{\frac{9}{4}}$. This translates into extremely high element counts and thus immense computing resources. The computational cost required to run a fully resolved DNS makes this type of simulation impractical for real flows that contain complex geometries and flow structures as well as high Reynolds number flows. To

give an idea of the overall computational cost of DNS, some respective Reynolds numbers are shown below.

Flows	Characteristic Velocity $\left(\frac{m}{s}\right)$	Reynolds Number (Re)	Required Mesh Points (N) for DNS
Model Airplane	1	$\approx 7 \times 10^4$	$\approx 8 \times 10^{10}$
Car	3	$\approx 6 \times 10^5$	$\approx 10^{13}$
Airplane	30	$\approx 2 \times 10^7$	$\approx 2 \times 10^{16}$
Atmospheric	?	$\approx 10^{20}$	$\approx 10^{45}$

Table 1.1: Representative Reynolds Numbers for DNS

In RANS, the entire momentum equation is time averaged in order to solve for the mean velocity field instead of the instantaneous velocity field. The time average yields an additional, non-linear term, called the Reynolds stress. The additional Reynolds stress term is unknown, so it must therefore be modeled. There are many different turbulence models that have been developed over the years, often times giving rise to even more unknowns that result in additional modeling. If an accurate model is obtained, this type of simulation is the easiest, fastest, and least expensive, however, with many variables continuing to be modeled, a lot of doubt can arise in the results.

LES is essentially a hybrid of DNS and RANS in which the larger turbulent scales are directly resolved without the use of any models while the smaller turbulent scales are modeled. Because of the explicit representation of the large scale, unsteady motions, LES is deemed more accurate and reliable than RANS [24], though it is computationally more expensive.

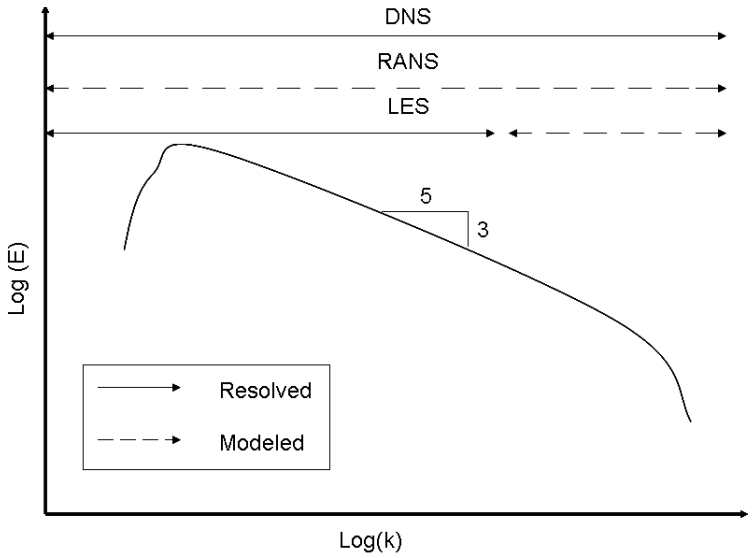

Figure 1.2: Wavelength vs. energy spectrum. Showing which turbulent eddy scales DNS, RANS, and LES resolve and model

1.3 Supercomputing

For real engineering problems, both geometries and flows can be very complex. As stated before, high Reynolds number flows dictate that simulations have many elements where the numerical solution to the Navier-Stokes equations is solved. With large numbers of elements and calculations needed leading to rising computation costs, more powerful computers are needed to handle even the simplest CFD problems. Thus, supercomputers are used to solve CFD problems. Supercomputers are systems with massive numbers of processors, typically ranging from several hundred to several hundred thousand, and high speed memory resources. The efficiency of such systems relies on the ability of the different processors to communicate with each other, called parallel processing. Parallel processing allows the problem to be split among all the processors while running simultaneously, reducing the time required to solve the problem.

1.4 Statement of Purpose

The ability to run simulations greatly enhances the design process by limiting the number of prototypes and experiments needed to improve an engineering design. Going forward, LES is the best numerical approach to design simulations that require a high level of accuracy while being able to balance cost. However, even with current supercomputing technology, the grid scaling requirement based on Reynolds number severely limits the applicability of LES in real engineering applications.

The objective of this study is to test the accuracy and speed increase of a basic wall model with the pre-existing massively parallel, spectral element code, Nek5000, and validate the model though characterizing turbulent flow behavior in a channel. The major setback to numerical simulations is the computational cost associated with them and the trade-off that must be made between computational cost and simulation accuracy. The accuracy associated with LES as well as the spectral accuracy and scaling capabilities of the present code can effectively be used while drastically reducing the required number of elements needed by means of a successful implementation of a wall model.

2 LITERATURE REVIEW AND NUMERICAL METHODS

In wall bounded flows, the region near a wall is of great importance and also difficult to handle. In the presence of a wall, a layer of fluid that is greatly influenced by the effects of viscosity, called a boundary layer, forms. Within the boundary layer, the sizes of the eddies that carry turbulent motion scale roughly as the distance away from the wall. In the near-wall region, the distance from the wall is defined by wall units;

$$y^+ = \frac{u_\tau y}{\nu} \tag{2.1}$$

$$u_\tau = \sqrt{\frac{\tau_w}{\rho}} \tag{2.2}$$

where u_τ is the friction velocity, τ_w is the wall shear stress, ρ is the density, and ν is the viscosity. Wall modeling is an approach in which the region near the wall is not resolved like the rest of the flow. Instead, it is modeled using various approaches in order to account for the effects of the unresolved turbulent scales while allowing the grid to scale with the larger turbulent scales in the outer flow region. In doing this, the number of grid points needed reduces significantly and makes the cost of the simulation only slightly dependent on the Reynolds number. Over the years, several distinct approaches to wall modeling have been implemented including the approximate boundary conditions approach, the Two Layer Model approach, and a Hybrid RANS/LES method.

2.1 Literature Review

In order to circumvent the computational restrictions associated with LES, Deardorff [7], in 1970, bypassed the inner layer while simulating turbulent channel flow at high Reynolds numbers through the use of approximate boundary conditions similar to RANS. Deardorff's boundary conditions forced the existence of a layer where the stress was constant, the logarithmic layer, as well as assumed that the turbulent fluctuations were isotropic. The assumption was based on the total average stress within the inner part of a boundary layer being almost constant. The boundary conditions are presented as;

$$\frac{\partial^2 \bar{u}}{\partial y^2} = -\frac{1}{\kappa \left(\frac{\Delta y}{2}\right)^2} + \frac{\partial^2 \bar{u}}{\partial z^2} \tag{2.3}$$

$$\bar{v}_w = 0 \tag{2.4}$$

$$\frac{\partial^2 \bar{w}}{\partial y^2} = \frac{\partial^2 \bar{w}}{\partial x^2} \tag{2.5}$$

By applying a no penetration condition on the wall-normal velocity at the wall and restricting the second derivatives of u and w at the first grid point off the wall, he related the velocity in the outer layer to the shear stress at the wall. The first boundary condition requires that the average velocity satisfies the log law while the no penetration condition helps satisfy continuity as well as implies that the Reynolds stress components $\bar{u}\bar{v}$, $\bar{v}^2$, and $\bar{v}\bar{w}$ at the wall are zero. Deardorff's model was incomplete because it assumed that solely the sub-grid scales were responsible for the shear stress at the wall as well as not having an effect on the Reynolds number essentially making it an infinite Reynolds number model.

In 1976, Schumann [27] altered Deardorff's approximated boundary conditions and simulated a turbulent channel using a finite volume approach. Schumann set a

condition on the shear stress at the wall, directly applying a linear relation between the stress and the velocity at the first grid point off the wall while still applying a no penetration condition at the wall.

$$\tau_{12,w}(x,z) = \left[\frac{\bar{u}(x,y_2,z)}{\langle\bar{u}(x,y_2,z)\rangle}\right]\langle\tau_w\rangle \tag{2.6}$$

$$\bar{v}_w = 0 \tag{2.7}$$

$$\tau_{32,w} = \left(\frac{2}{Re_\tau}\right)\left[\frac{\bar{w}(x,y_2,z)}{y_2}\right] \tag{2.8}$$

where $\langle\rangle$ represents the time average and y_2 is the location of the first grid point off the wall, which must be located outside the inner region. In the first condition, the mean velocity $U(y_2) = \langle\bar{u}(x,y_2,z)\rangle$ is obtained through the log law while $\langle\tau_w\rangle$, the average wall stress, is solved for using a global momentum balance. In a channel flow, the average wall shear stress is set equal to the pressure gradient driving the flow.

Grötzbach [11] modified Schumann's approach by averaging the the axial velocity at the first grid point off the wall over the entire plane parallel to the wall. He then estimated $\langle\tau_w\rangle$ with the log-law using the calculated, planar averaged velocity as the input value and solved for u_τ.

$$u^+(y_2) = \frac{U(y_2)}{u_\tau} = 2.5log\left(\frac{y_w u_\tau}{\nu}\right) + 5.2 \tag{2.9}$$

where y_w is the distance from the wall to the first grid point. The benefits of Grötzbach's modifications were that the pressure gradient no longer needed to be known beforehand in order to close the model. By iteratively solving for the average wall shear stress, fluctuation in both the pressure gradient and the mass flux is allowed instead of prescribing and fixing both quantities.

In 1989, Piomelli [23] proposed new approximate boundary conditions that correlated the wall stress and the instantaneous velocity downstream using a streamwise displacement as well as took into account sweep and ejection events within the flow.

$$\tau_{12,w}(x,z) = \langle \tau_w \rangle - C u_\tau \bar{u}(x + \Delta_s, y_2, z) \tag{2.10}$$

$$\bar{v}_w(x,z) = 0 \tag{2.11}$$

$$\tau_{32,w}(x,z) = \left[\frac{\langle \tau_w \rangle}{U(y_2)} \right] \bar{w}(x + \Delta_s, y_2, z) \tag{2.12}$$

$$\Delta_s = (1 - |y_2|) \cot\theta \tag{2.13}$$

$$\theta = \begin{cases} 8^\circ : & 30 < y_2^+ < 50 - 60 \\ 13^\circ : & y_2^+ > 60 \end{cases} \tag{2.14}$$

where Δ_s is the streamwise displacement, $\langle \tau_w \rangle$ is obtained from the log law, and C is a dimensionless constant of order 1. The addition of a streamwise displacement improved the correlation of velocity and wall stress by taking the inclination of elongated structures into account. The stretching of vortex structures and increase in fluid turbulence near the wall is due to the impingement of the higher velocity fluid which increases the wall stress. At the same time, ejection of energy and structures needs to be accounted for due to its reduction of the the stress at the wall. The value of θ varies with y^+ in the inner layer and can be found experimentally in the works of Rajagopalan and Antonia [25].

These new approximate boundary conditions saw a good improvement over the ones previously used. Other modifications have also been made using the approximate boundary condition approach. Werner and Wengle [28] chose to fit the power-law profiles for the streamwise velocity instead of the log-law. The power-law can be inverted explicitly, which aids in numerical computations. Other modifications

include accounting for the effects of buoyancy [18], wall roughness [17], and control theory and using linear stochastic estimation [19, 2] in order to obtain the wall shear stress. Wu and Squires [29] used a slightly different approach in which they solved for u_τ with a separate RANS calculation while solving for the flow over a rounded bump.

The approximate boundary condition approach supplied good results for primarily simple geometries such as channels, however, they rely on a crucial assumption that the fluid turbulence is in equilibrium. In more complex geometries such as diverging or rotating channels, or geometries that produce strong pressure gradients or secondary flows such as separation and re-circulation, these models have had very limited success, if any, while often failing immensely. This lead to the the Two Layer Model (TLM), shown in Figure 2.1. TLM essentially solves a separate set of equations on a second, embedded grid within the near-wall region.

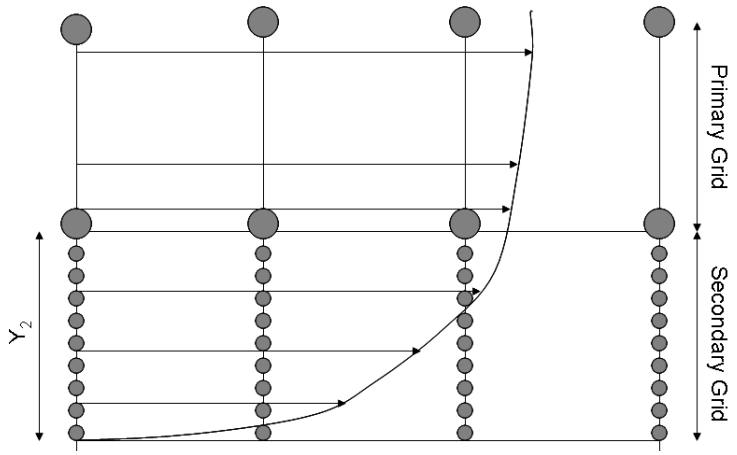

Figure 2.1: Two Layer Model grid structure.

The Two Layer model uses an outer layer grid based on LES grid requirements while, in the near-wall region, a second embedded grid is established within the first

cell of the LES grid, at the wall. On the is secondary grid, a separate set of equations is solved and the value of the velocity field is used as a Dirichlet boundary condition to the LES grid. Balaras, Benocci, and Piomelli [3] solved a system derived from the boundary layer equations on the secondary grid.

$$\frac{\partial \bar{u}_i}{\partial t} + \frac{\partial}{\partial x}\left(\bar{u}_1 \bar{u}_2\right) + \frac{\partial}{\partial z}\left(\bar{u}_3 \bar{u}_1\right) = -\frac{\partial \bar{p}}{\partial x_i} + \frac{\partial}{\partial z}\left(\left(\nu + \nu_{SGS}\right)\frac{\partial \bar{u}_i}{\partial z}\right), i = 1, 2 \tag{2.15}$$

$$\nu_{SGS} = \left(\kappa z\right)^2 D_b(z)|\bar{S}| \tag{2.16}$$

$$D_b(z) = \left(1 - \exp\left(-\left(\frac{z^+}{A^+}\right)^3\right)\right) \tag{2.17}$$

where z is the wall normal direction, κ is the Von Karman constant, $D_b(z)$ is a damping function, and $A^+ = 25$. Cabot [4, 5] proposed a different definition:

$$\nu_{SGS} = \kappa u_s z D_C^2(z) \tag{2.18}$$

$$D_C(z) = \left(1 - \exp\left(-\frac{z u_d}{A\nu}\right)\right) \tag{2.19}$$

where u_s and u_d are determined velocity scales and $A = 19$.

The third method of wall modeling is a Hybrid RANS/LES approach. This method is similar to the TLM, however, instead of a using a separate embedded grid, this method has a single grid which is divided into zones. This method solves the LES equations in the outer zone while solving a set of RANS equations in the near-wall zone and the two zones are weakly coupled together at a matching point. The difficulty with this approach is the buffer region that is created where the two zones meet. Matching the different turbulent scales provided by each set of equations is a challenge. Baggett [1] used two models in order to explicitly blend the two regions together in a smooth transition. The first uses a linear combination of the predicted

turbulent/subgrid stresses while taking anisotropy of fluid turbulence into account:

$$\tau_{ij} - \frac{1}{3}\tau_{kk}\delta_{ij} = -\nu_{SGS}\left[S_{ij} - (1-\beta(z))\left\langle \bar{S}_{ij}\right\rangle\right] - \beta(z)\nu_{RANS}\left\langle \bar{S}_{ij}\right\rangle \tag{2.20}$$

where ν_{SGS} and ν_{RANS} are the LES sub-grid and RANS turbulent viscosities respectively and $\beta(z)$ is a prescribed function of distance to the wall. The second method blends the modeled viscosities.

$$\tau_{ij} - \frac{1}{3}\tau_{kk}\delta_{ij} = \left[(1-\beta(z))\,\nu_{SGS} + \beta(z)\nu_{RANS}\right]\bar{S}_{ij} \tag{2.21}$$

Using either method of smoothing, $\beta = 0$ corresponds to a classical LES while $\beta = 1$ yields a classical RANS simulation.

While all of the previously mentioned approaches and models have been implemented successfully at some point in time, this current work will focus on a very simple model based on the approximate boundary condition approach. The desire is to test the speed increase and accuracy of the wall model combined with the present spectral element code, Nek5000. Upon successful test, future works can begin incorporating more sophisticated models for a wider spectrum of problems.

2.2 Numerical Method

The governing equations for an incompressible and Newtonian fluid flow are given by the Navier-Stokes equations shown here in tensor notation,

$$\frac{\partial u_i}{\partial t} + \frac{\partial\left(u_i u_j\right)}{\partial x_j} = -\frac{1}{\rho}\frac{\partial P}{\partial x_i} + \nu\frac{\partial^2 u_i}{\partial {x^2}_j} \tag{2.22}$$

$$\frac{\partial u_j}{\partial x_j} = 0 \tag{2.23}$$

where ρ is the density, ν is the kinematic viscosity, and u_i is the j_{th} component of the velocity field. The incompressible assumption defines a constant density while the Newtonian fluid assumption sets a relationship of the shear stress, τ, to the strain rate, $\frac{\partial u}{\partial y}$, through the proportionality constant, μ, being the dynamic viscosity, $\tau = \mu\frac{\partial u}{\partial y}$. The three components of velocity, represented by the j_{th} component, are the x, y, and z Cartesian coordinates. A spatial filtering operation is performed to decompose the exact (DNS) equations into filtered (LES) equations,

$$\overline{f}(x) = \int G(x, x')f(x')dx' \tag{2.24}$$

where G is a filter function and the integral is taken over the entire flow domain In theory, the filter function is applied to the original Navier-Stokes equations in order to to decompose the velocity field into the sum of a filtered (resolved) component and unfiltered (residual) component. However, the filter is almost never solved for and is instead represented as another function (The most commonly used filters are presented in Pope [24]). The resolved component represents the larger scale, higher energy containing motions while the residual component represents the smaller scale, lower energy containing motions to be modeled. The result is the incompressible LES equations;

$$u(x,t) = \bar{u}(x,t) + u'(x,t) \tag{2.25}$$

$$\frac{\partial \bar{u}_i}{\partial t} + \frac{\partial\left(\bar{u}_i\bar{u}_j\right)}{\partial x_j} = -\frac{1}{\rho}\frac{\partial \bar{P}}{\partial x_i} + \nu\frac{\partial^2 \bar{u}_i}{\partial {x^2}_j} - \frac{1}{\rho}\frac{\partial \tau_{ij}}{\partial x_j} \tag{2.26}$$

$$\frac{\partial \bar{u}_j}{\partial x_j} = 0 \tag{2.27}$$

where the overbar represents the filtered variable and $\tau_{ij} = \rho\left(\overline{u_i u_j} - \bar{u}_i\bar{u}_j\right)$ is the SGS stress tensor produced by the filtering operation and reorganizing terms. The SGS

stress cannot be solved with the larger, resolved scales, but the assumption that the smaller eddies are universal and their effect is negligible in the total production of turbulent energy [20], allows it to be modeled.

2.2.1 Eddy Viscosity Model

The most common approach to model the SGS stress is the linear eddy viscosity assumption. This assumption relates the the residual stress to the strain rate tensor of the filtered velocity field through a proportionality constant;

$$\tau_{ij} \approx \nu_T \overline{S_{ij}} \tag{2.28}$$

where ν_T is the eddy viscosity of the residual motions and $\overline{S_{ij}} = \frac{1}{2}\left(\frac{\partial \bar{u}_i}{\partial x_j} + \frac{\partial \bar{u}_j}{\partial x_i}\right)$ is the strain rate tensor. It is important to note that the eddy viscosity is not a property of the fluid, but of the flow itself [20]. Though many different models for the eddy viscosity term exist, the most commonly used model is the Smagorinski model.

The Smagorinski model dictates that the eddy viscosity is proportional to the characteristic length and velocity of the small scales while assuming that the SGS kinetic energy and production are balanced by the rate dissipation. This implies that the smaller scales are in a state of equilibrium. The Smagorinski model defines the eddy viscosity as

$$\nu_T = {\ell_s}^2 \bar{S} = (C_s \Delta)^2 \bar{S} \tag{2.29}$$

where $\bar{S}$ is the characteristic filtered strain rate, C_s is the Smagorinski coefficient, Δ is the filter width, and the Smagorinski length scale, ℓ_s, is proportional to the filter width through the Smagorinski coefficient, which is analogous to the mixing-length hypothesis [24] developed by Prandtl. By estimating $\bar{S}$ from the Kolmogrov

spectrum, a value of the Smagorinski constant $C_s \approx 0.17$ was found. This model worked reasonably well for homogeneous, isotropic turbulence with cutoff in the inertial subrange [9], however, in inhomogeneous flows, such as wall bounded flows, the value was too large causing the eddy viscosity to dissipate too much energy by dampening the large-scale fluctuations. Excessive dampening of the larger, resolved scales changes the overall the flow field, especially in transitional flows where the growth rates of the initial perturbations was found to be inaccurate.

In order to more accurately model eddy viscosity, a dynamic approach was created in order to calculate the eddy viscosity coefficient locally, adapting to the present flow conditions. The model uses information from the smallest resolved scales to model the sub-grid stresses. In theory, the Dynamic Smagorinski model, used in the present code, defines two filter operations that are applied to the Navier-Stokes equations, a grid filter $\bar{G}$, and a test filter $\tilde{G}$, where the test filter width is larger than the grid filter width.

$$\overline{f}(x) = \int G(x, x') f(x') dx' \tag{2.30}$$

$$\tilde{f}(x) = \int \tilde{G}(x, x') f(x') dx' \tag{2.31}$$

$$\tilde{\bar{G}} = \tilde{G}\bar{G} \tag{2.32}$$

The grid filter is applied to the Navier-Stokes equations forming the LES equations, where the effects of the scale scale are present in the SGS stress term $\tau_{ij} = \overline{u_i u_j} - \bar{u}_i \bar{u}_j$.

Applying $\tilde{\bar{G}}$ to the LES equations generates a new set of filtered LES equations;

$$\frac{\partial \tilde{\bar{u}}_i}{\partial t} + \frac{\partial \left(\tilde{\bar{u}}_i \tilde{\bar{u}}_j\right)}{\partial x_j} = -\frac{1}{\rho}\frac{\partial \tilde{\bar{p}}}{\partial x_i} + \nu \frac{\partial^2 \tilde{\bar{u}}_i}{\partial {x^2}_j} - \frac{1}{\rho}\frac{\partial T_{ij}}{\partial x_j} \tag{2.33}$$

$$T_{ij} = \widetilde{\overline{u_i u_j}} - \tilde{\bar{u}}_i \tilde{\bar{u}}_j \tag{2.34}$$

$$L_{ij} = \widetilde{\bar{u}_i \bar{u}_j} - \tilde{\bar{u}}_i \tilde{\bar{u}}_j = T_{ij} - \tilde{\tau}_{ij} \tag{2.35}$$

where the sub-grid scale stress is now T_{ij} and the turbulent stress from the resolved scales whose length fall between the grid filter and test filter width is L_{ij}. Two more variables, M_{ij} and m_{ij} are defined to model the anisotropic parts of T_{ij} and τ_{ij} respectively.

$$\tau_{ij} - \frac{\delta_{ij}}{3}\tau_{kk} \simeq m_{ij} = -2C\bar{\Delta}^2 |\bar{S}| \bar{S}_{ij} \tag{2.36}$$

$$T_{ij} - \frac{\delta_{ij}}{3}T_{kk} \simeq M_{ij} = -2C\tilde{\bar{\Delta}}^2 |\tilde{\bar{S}}| \tilde{\bar{S}}_{ij} \tag{2.37}$$

$$\tilde{\bar{S}}_{ij} = \frac{1}{2}\left(\frac{\partial \tilde{\bar{u}}_i}{\partial x_j} + \frac{\partial \tilde{\bar{u}}_j}{\partial x_i}\right) \tag{2.38}$$

$$|\tilde{\bar{S}}| = \sqrt{2\tilde{\bar{S}}_{mn}\tilde{\bar{S}}_{mn}} \tag{2.39}$$

where $\bar{\Delta}$ is the characteristic filter width related to $\bar{G}$ and $\tilde{\bar{\Delta}}$ is the characteristic filter width related to $\tilde{\bar{G}}$.

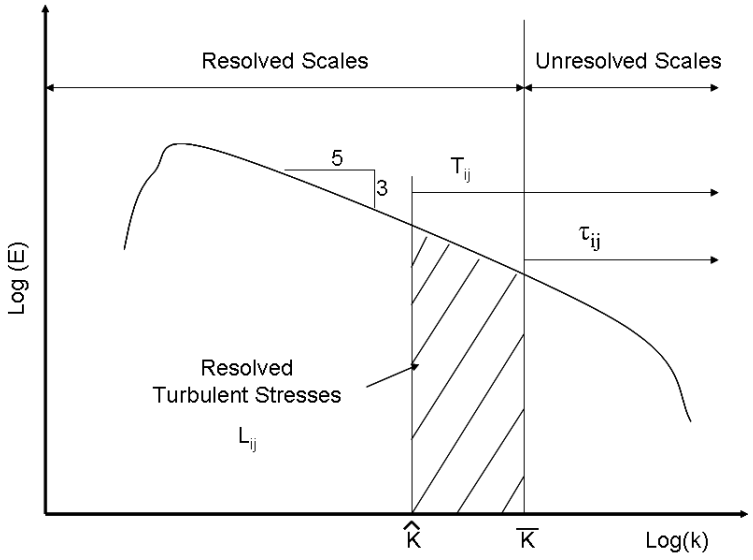

Figure 2.2: Dynamic smagorinski filter. The Dynamic smagorinski model uses both a grid and test filter to model the smallest scales.

The Smagorinski coefficient, C, is assumed to be only a function of y and t in channel flow to avoid and indeterminate value while a planar average is taken on the plane parallel to the wall. The result is;

$$C(y,t) = -\frac{1}{2}\frac{\left\langle L_{ij}\bar{S}_{ij}\right\rangle}{\tilde{\bar{\Delta}}^2\left\langle|\tilde{\bar{S}}|\tilde{\bar{S}}_{mn}\bar{S}_{mn}\right\rangle - \bar{\Delta}^2\left\langle|\tilde{\bar{S}}|\tilde{\bar{S}}_{pq}\bar{S}_{pq}\right\rangle} \tag{2.40}$$

$$m_{ij} = \frac{\left\langle L_{ij}\bar{S}_{ij}\right\rangle}{\frac{\tilde{\bar{\Delta}}}{\bar{\Delta}}^2\left\langle|\tilde{\bar{S}}|\tilde{\bar{S}}_{mn}\bar{S}_{mn}\right\rangle - \left\langle|\tilde{\bar{S}}|\tilde{\bar{S}}_{pq}\bar{S}_{pq}\right\rangle}|\bar{S}|\bar{S}_{ij} \tag{2.41}$$

where m_{ij} is the dynamic eddy viscosity sub-grid scale stress model. The dynamic model scales as the cube of the distance to the wall in the near-wall region, accurately describing the asymptotic behavior of the SGS stress tensor [9]. The model also allows for backscatter, the energy that flows from the small scales to the large scales. This is a phenomenon that the original Smagorinski model did not account for and in some cases should not be ignored. The dynamic Smagorinski model allows ν_t to

vanish as the wall is approached, where only the molecular viscosity should have a contribution. Essentially, the dynamic Smagorinski model using information from the smallest resolved scales in order to model to smallest turbulent motions, as shown in Figure 2.2.

2.3 Numerical Solution: Spectral Element Method

To solve partial differential equations such as the Navier-Stokes equations, the technique of approximating the solution through the use of continuous functions is used. Typically these functions are polynomials whose derivatives are required to satisfy the governing equations at discrete (grid) points. The approximation technique used by the present code, Nek5000, is the spectral element method (SEM). The spectral element method is a high-order, weighted residual technique similar to the finite element method (FEM). Similar abilities handling complex geometries and being capable of local mesh refinement through h-refinement, increasing the number of elements, or p-refinement, increasing the polynomial order within the elements are achievable. The order of a method refers to the order of the polynomials used in the approximation of the solution. Both methods split the entire domain into smaller elements in which the solution is approximated. An essential condition however, is that the solution matches at the boundaries of adjacent elements. Deville [8] refers to each individual element in the domain as a parent element where the nodes on the boundaries of each element are referred to as primary or element boundary nodes. Each parent element spans a length of 2, from [-1, 1], in one dimension while the same principle extends to the second and third dimensions. The coordinates, ξ, in each parent element are mapped using a transformation. Within each parent element, the

approximate solution takes the form of

$$u^e = u_N^e(\xi) = \sum_{n=0}^{N} a_n \phi_n(\xi) \tag{2.42}$$

where ϕ_n are interpolation polynomials, a_n are coefficients that need to be solved for, and N is the polynomial order used in each parent element. The interpolation polynomials take the form of

$$\phi(\xi) = \prod_{i \neq n} \frac{\xi - \xi_i}{\xi_n - \xi_i} \tag{2.43}$$

The mapped points ξ_n, called secondary points and corresponding to each value a_n, are the points in each parent element to which the function is interpolated. Each polynomial is characterized as having a value of zero at every point except the point corresponding to its own number, where it has a value of one. This allows the coefficient, a_n to be the solution at each point.

$$\phi_n(\xi_j) = \begin{cases} 1: & j = n \\ 0: & j \neq n \end{cases} \tag{2.44}$$

The number of secondary grid points in directly related to the polynomial order. The higher the order of the method used, the more secondary points and interpolating polynomials each parent element has. FEM algorithms typically only use up to 2nd order elements requiring that if more accuracy is needed, the number of elements must increase, also called h-refinement. SEM, implementing high-order schemes in nature, allows the option of increasing the polynomial order yielding more secondary grid points within each element if greater accuracy is required. This is called p-refinement. A major difference between the two methods also comes from

how orthogonality of the polynomials is defined. In FEM, the orthogonality between the basis functions is uniquely due to non-overlapping local functions. Conversely, in SEM, orthogonality is related to both the topological nature (local extension) and the analytical nature of the basis functions [8]. Chebyshev (T_n) or Legendre (L_n) polynomials are examples of orthogonal basis functions used to approximate the solution for the entire domain. Due to more straightforward implementation of Legendre polynomials, they are typically chosen over the use of Chebyshev polynomials. The reason that higher order schemes become problematic for the FEM, and not SEM, has to do with the spacing of the secondary grid points. FEM uses uniform grid spacing for the secondary points causing the polynomials to overshoot the endpoints, leading to large errors. SEM, however, uses non-uniform interpolation points where the points are the solutions to;

$$\left(1-\xi^2\right) L'_N(\xi) = 0 \tag{2.45}$$

L'_N is the derivative of the Legendre polynomial with the highest order existing within the element. These new solution points are called Gauss-Lobatto-Legendre (GLL) points. This technique results in the distance between the GLL points decreasing as you move away from the center of the element. The concentration of points near the endpoints results in reducing the error in overshooting that the polynomials have compared to uniformly spaced points. Figure 2.3 shows a comparison of a uniformly spaced finite element and a non-uniformly spaced spectral element, demonstrates the reduced error in interrelation accuracy. The elements are both 8th order elements, the same order elements used in the present simulation.

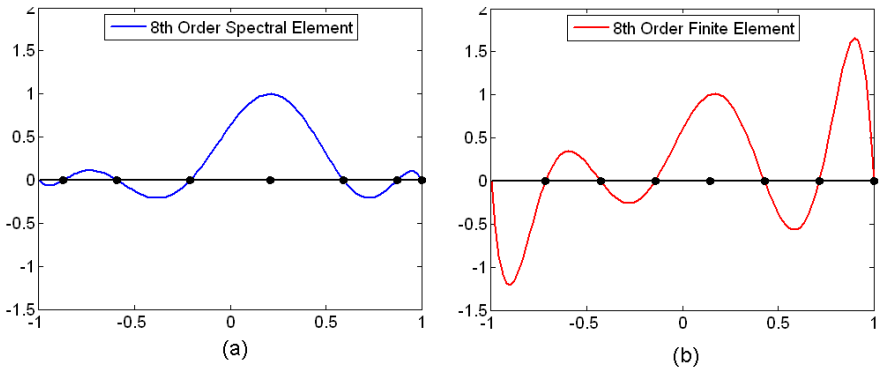

Figure 2.3: Interpolation polynomials. An 8th Order Spectral Element (a) and an 8th Order Finite Element (b), each showing the 5th polynomial.

Another benefit to SEM is the convergence rate, shown in Figure 2.4. The convergence rate is essentially, given an accuracy requirement, how many grid points the scheme will need in order to reach the given accuracy. While FEM typically has a second order rate of convergence, SEM has an exponential rate that allows it to use far fewer grid points to produce the same accuracy.

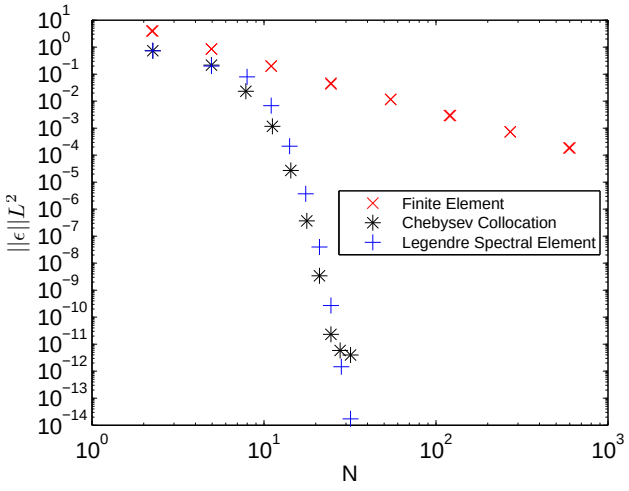

Figure 2.4: Spectral convergence as a function of degrees of freedom. The L^2 error norms as a function of the number of degrees of freedom, N.

This characteristic is very important when applying SEM to real problems because it reduces the amount of computing time, thus computational cost, needed to solve complex problems. For more in-depth information on spectral elements, the reader is invited to reference Deville [8].

2.4 Nek5000

Nek5000 is an open source, high-order, massively-parallel, spectral element CFD code that brings together the essential characteristics of speed and accuracy needed for solving the Navier-Stokes equations. While primarily used in academic research at this point; in time, Nek5000 could be a substantial design tool given its ability to cover a broad range of applications including combustion modeling, thermal hydraulics, and general fluid flow. From the beginning, Nek5000 was built to optimize speed and accuracy capabilities allowed by the spectral element method as well as originally being designed to take advantage of parallel computing, currently being able to scale to over 250,000 processors [21]. As a parallel code, it uses efficient element-to-element communication while using high-order elements to improve accuracy. Originally designed as a DNS solver by default, Nek5000 allows additional user input and modification to add routines ranging anywhere from turbulence models to post-processing calculations, allowing, in this case, the transformation into an LES solver.

Aside from the source code, Nek5000 uses three additional files in order to set up a problem, *SIZE* file, *rea* file, and the *usr* file. The *SIZE* file contains information important to the number of processors to use, the division of elements per processor, the polynomial order of the Legendre polynomial basis functions, and whether a PN/PN or PN/PN-2 method will be used. The difference between these two methods is how the code handles solving for pressure. The *rea* file stores all the fluid

properties, mesh information, time-stepping information, and number of time-steps to be run. The *usr* file is where you can add additional routines for the solver to run, as well as set boundary and initial conditions. In the present study, modifications to the source code and additions to the *usr* file were the primary focus for a successful wall model implementation.

In the *usr* file, several base functions are defined and called by the source code during a simulation. The primary functions of interest are the *userbc()* function and the *userchk()* function. The *userbc()* function, as one might guess, allows the user to set values or functions that define the boundary conditions. In the present study, this is where the the no penetration condition, $v = 0$ at the wall, and the values of stress at the walls are defined and applied to the numerical solution. The *userchk()* function, called at every time-step, is where the user can define functions for post-processing such as averaging routines or calculate other quantities of interest, as well as adding routines that can modify the flow field such as turbulence models or adding acceleration to an outflow boundary to avoid numerical complications. In the present study, this function is where the eddy viscosity for the turbulence model is calculated through a defined routine, *eddy_visc*. The function, *eddy_visc*, is where the values for the Dynamic Smagorinski model are calculated and applied to the discretized equations to be solved numerically. The modifications to the source code required to implement the wall model will be discussed later in the Test Case section.

2.5 Wall Modeling Theory

In a well-resolved LES, the grid required is almost as fine as one needed to perform a DNS. An accurate LES with the near-wall region and the needed turbulent scales resolved requires a number of grid points that scales as $N \sim {Re_\tau}^2$, where Re_τ is the friction Reynolds number. To accurately represent the structures in the near-

wall region, the first grid point must be located at $y^+ < 1$, and the grid spacing must be of order $\Delta x^+ \simeq 50 - 150$, $\Delta z^+ \simeq 15 - 40$ [22]. As $Re \to \infty$, the number of grid points must increase to avoid or lessen numerical inaccuracy. Using wall models can help relax the grid spacing requirements through modeling the wall layer by correlating the wall stress with the outer layer velocity field using a specified law relation. When using a model, the first grid point off the wall is placed in the outer flow layer, $y^+ \simeq 30 - 200$, since the small, turbulent structures do not need to be resolved. Approximated boundary conditions are applied at the wall that correlate the outer flow with the wall shear stress while the necessary assumptions are applied. This also allows coarser mesh in the x and z directions, $\Delta x^+ \simeq 100 - 600$, $\Delta z^+ \simeq 100 - 300$, drastically reducing the required number of elements needed.

2.5.1 Log-Law

According to Pope [24], it is useful to divide the flow into three regions, the viscous wall region ($y^+ < 50$), the log-law region ($50 < y^+ \simeq 285$), and the core ($y^+ > 285$). The value of 285 corresponds to the Reynolds number of the present simulation, ($Re_\tau = 950$). Furthermore, the viscous wall region can be subdivided to three main, distinct regions; the viscous sub-layer, the buffer layer, and the inertial sub-layer. Each of these regions are characterized by the effects and contributions of both viscosity and the Reynolds stresses to the total stress, as shown in Figure 2.5. The viscous contribution drops from 100% at the wall ($y^+ = 0$) to 50% at $y^+ \approx 12$ and is less than 10% by $y^+ = 50$ [24].

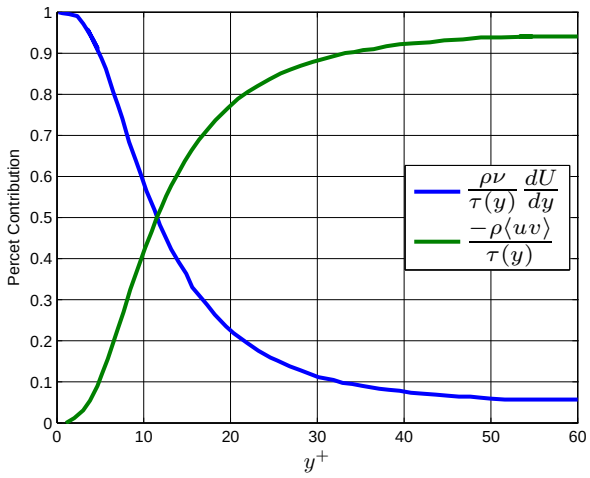

Figure 2.5: Fractional stress contributions. The viscous stress and Reynolds stress have different fraction contributions to the total shear stress depending on y^+, as seen in Pope [24]

Prandtl suggested that the viscous wall region, or inner layer, is characterized as a region where the mean velocity profile is independent of U_0, the centerline velocity, and δ, the outer layer length scale, and only determined by the effects of the viscous scales. Within the Inner layer, u^+ is defined as only a function of y^+, according to Prandtl's hypothesis, and is expressed as;

$$u^+ = \frac{\langle U \rangle}{u_\tau} \tag{2.46}$$

The law of the wall defines u^+ as an integral function of y^+;

$$\frac{du^+}{dy^+} = \frac{1}{y^+}\Phi_I(y^+) \tag{2.47}$$

$$u^+ = \int_0^{y^+} \frac{1}{y'}\Phi_I(y')dy' \tag{2.48}$$

where Φ_I is a function of $\frac{y}{\delta}$ and y^+ that tend asymptotically to a function of y^+ only,

as $\frac{y}{\delta}$ tends to zero [24].

- Viscous Sub-Layer: $0 < y^+ < 5$

In this region, the Reynolds stress is negligible compared to the viscous stress, however, experiments have shown that a small fraction of the Reynolds stress still remains up to about $y^+ = 5$. In this region, through integration, the relationship $u^+ = y^+$ is obtained.

- Buffer Layer: $5 < y^+ < 30$

This is essentially a transition region between viscous-dominated and turbulence-dominated regions of the the flow where neither the viscous stress nor the Reynolds stresses can be neglected.

- Inertial Sub-Layer: $30 < y^+ \simeq 285$

This region is called the log-law region due to the logarithmic nature of the mean velocity profile. Data has shown that the Reynolds number has an impact on the size of this region. The higher the Reynolds number is, the further this region reaches in terms of values of y^+. In this region, the velocity gradient is,

$$\frac{du^+}{dy^+} = \frac{1}{\kappa y^+} \tag{2.49}$$

which integrates to

$$u^+ = \frac{1}{\kappa} \ln y^+ + B \tag{2.50}$$

where κ is the von *Kármán* constant and B is a constant based on the intersection of the slope. Through vast amounts of experiments and literature, the values of these

two constants varies slightly, however, they generally fall within ±5% of the values,

$$\kappa = 0.41 \tag{2.51}$$

$$B = 5.2 \tag{2.52}$$

Typically, for the approximate boundary condition method, the first grid point off the wall is placed somewhere within the log-law region so that the log-law can be directly applied to the grid point in accordance with the law of the wall, shown in Figure 2.6.

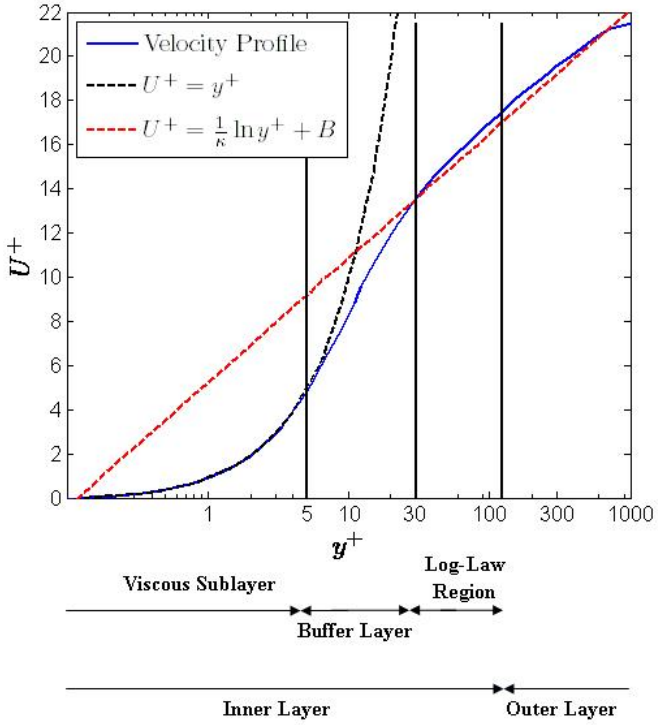

Figure 2.6: Law of the wall. The different algebraic relationships for each individual region of the inner layer

The viscous wall region contains the most vigorous turbulent activity. The pro-

duction, dissipation, turbulent kinetic energy, and anisotropy all achieve their peak values at $y^+ < 20$ [24].

2.6 Test Case

The test case chosen to simulate this study of an LES with a wall model was flow through a turbulent channel at $Re_\tau = 950$ based on the friction velocity, u_τ and the channel half height h. The first step was to balance forces and derive the driving pressure force, $\frac{\partial P}{\partial x}$ in the channel where the mean centerline velocity $U = 1$, shown in Figure 2.7.

2.6.1 Balance of Forces

Beginning with a fully developed flow within the channel, meaning the velocity profile is the same everywhere along the direction of the flow, the continuity equation is simplified first. Assuming that there is no velocity in the z-direction, $w = 0$, and u does not vary in the x-direction, $\frac{\partial u}{\partial x} = 0$ since the flow is fully developed, the continuity equation reduces as follows,

$$\frac{\partial u}{\partial x} + \frac{\partial v}{\partial y} + \frac{\partial w}{\partial z} = 0 \tag{2.53}$$

$$\cancelto{0}{\frac{\partial u}{\partial x}} + \frac{\partial v}{\partial y} + \cancelto{0}{\frac{\partial w}{\partial z}} = 0 \tag{2.54}$$

$$\frac{\partial v}{\partial y} = 0 \tag{2.55}$$

In order to satisfy the no penetration condition that $v = 0$ at the walls, $v = 0$ must be true for all y values. The x-direction momentum equation applied to a differential control volume is similarly simplified to begin the analysis. As a result of the same assumptions and the simplified continuity equation, only the surface forces

remain and are equal to zero.

$$\rho\left(\frac{\partial u}{\partial t}+u\frac{\partial u}{\partial x}+v\frac{\partial u}{\partial y}+w\frac{\partial u}{\partial z}\right)=-\frac{\partial P}{\partial x}+\mu\left(\frac{\partial^2 u}{\partial x^2}+\frac{\partial^2 u}{\partial y^2}+\frac{\partial^2 u}{\partial z^2}\right) \tag{2.56}$$

$$\rho\left(\cancel{\frac{\partial u}{\partial t}}^{0}+u\cancel{\frac{\partial u}{\partial x}}^{0}+\cancel{v\frac{\partial u}{\partial y}}^{0}+\cancel{w\frac{\partial u}{\partial z}}^{0}\right)=-\frac{\partial P}{\partial x}+\mu\left(\cancel{\frac{\partial^2 u}{\partial x^2}}^{0}+\frac{\partial^2 u}{\partial y^2}+\cancel{\frac{\partial^2 u}{\partial z^2}}^{0}\right) \tag{2.57}$$

$$\frac{\partial P}{\partial x}=\mu\frac{\partial^2 u}{\partial y^2} \tag{2.58}$$

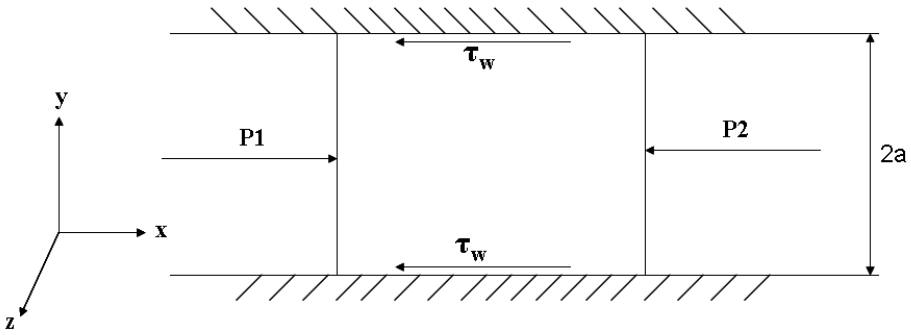

Figure 2.7: Balance of Forces in a Channel

This flow is purely driven by the pressure gradient with no flow acceleration added to the system. Therefore, the momentum equation results in the balance of the axial pressure gradient and the shear stress as seen above. With the shear stress only being a function of y, $\tau(y)$, and the driving pressure only being a function of x, it is clear that both variables have constant values. By integrating the relationship

along the y-direction evaluating y from [-1,1],

$$\frac{\partial P}{\partial x}\left(\frac{y^2}{2}\right) = \mu U \tag{2.59}$$

$$\frac{\partial P}{\partial x}\frac{y^{\cancel{2}^{1}}}{2} = \mu \cancel{U}^{1} \tag{2.60}$$

$$\frac{\partial P}{\partial x} = 2\mu \tag{2.61}$$

the resulting value of the pressure gradient is determined. This value is added as a source term driving the flow in the simulation. This value is defined in the *user* file in Nek5000 in the function *userf*.

2.6.2 Mesh Generation

After deriving the value of the driving pressure gradient, the computation domain and mesh needed to be created. Based on DNS data provided by Jimenez and Hoyas [13] (Discussions of Data and results can be found [14, 15, 16]), the following parameters, shown in Table 2.1, were assumed for the dimensions of the channel and necessary flow data values. For the basic wall model, these values are used from experimental data in order to appropriately implement the wall model, however, in more advanced wall models and later modifications, many of these values will be calculated from the flow itself and supplied directly to the boundary conditions.

X Length	$\frac{L_x}{h} = 8\pi$
Channel Half Height	$h = 2$
Z Length	$\frac{L_z}{h} = 3\pi$
Friction Reynolds Number	$Re_\tau = 950$
Friction Velocity	$u_\tau = 0.0454$
Viscosity	$\nu = 4.8591 \times 10^{-5}$
Experimental $y^+ = 100$	$y = 0.10678$
Velocity at $y^+ = 100$	$U_{exp} = 0.7462$

Table 2.1: Computational Domain Dimensions and Experimental Flow Values

Using the experimental values for u_{tau}, and ν, the value of y^+ in wall units was able to be calculated and used to create the necessary mesh. Recall that the use of a wall model allows the first grid point off the wall to be placed in the outer layer instead of requiring high resolution in the near-wall region. In a wall resolved LES, recall that the first grid point needs to be located with $y^+ < 1$. Typical LES grids will also require 2 points within $y^+ = 5$ and assign a growth rate of the element size in the wall normal direction, $\alpha = 1.1 - 1.3$ until $\Delta y^+ = 30$. Once $\Delta y^+ = 30$, the element size will be uniform. These rules of thumb are used in order to capture the required length scales. In this study, a conservative value of $y^+ = 100$ was chosen for the location of the first grid point and the element size, Δy^+, in the wall normal direction was uniform. Similarly, conservative values for Δx^+ and Δz^+ were chosen for the first iteration of the wall model and similarly had uniform element sizes. Table 2.2 shows the meshing values and required number of elements for the present wall modeled LES and a wall resolved LES (WR LES). Two runs with different grid spacing were used for the wall modeled case. Figure 2.8 shows the two meshes, a conservative approach using smaller grid spacing (WM LES) and a mesh with much

coarser grid spacing (LGWM LES) according to the requirements allowed by Piomelli [22] $\Delta x^+ \simeq 100 - 600$, $\Delta z^+ \simeq 100 - 300$.

Method	Δx^+_{max}	Δz^+_{max}	Δy^+_{max}	α	Number of Elements (XxYxZ)	Total Elements
WR LES	30	30	30	1.3	112×24×42	112896
WM LES	50	30	30	N/A	67×10×42	28140
LGWM LES	300	200	30	N/A	11×10×6	660

Table 2.2: Meshing Values

Recall that for a DNS, the number of elements needed to resolve all length scales goes as $N \sim Re^{\frac{9}{4}}$. This means a DNS would require approximately 7.16×10^5 elements. The conservative wall modeled LES reduces the number of elements needed by over 70% compared to the wall resolved LES and the coarse mesh case reduces the number of elements needed by close to 200 times.

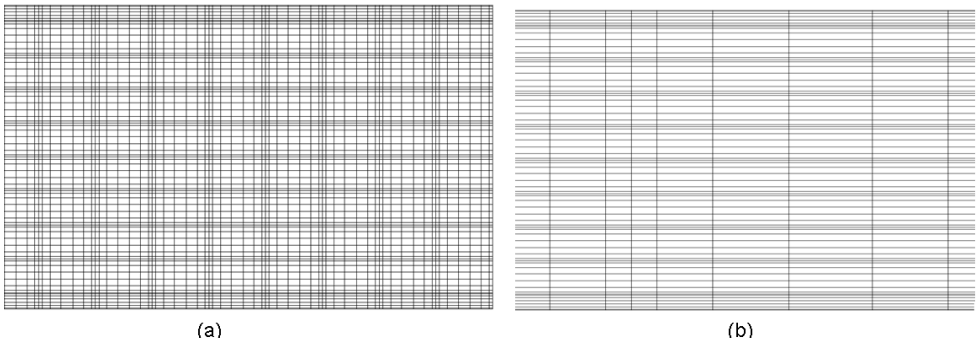

Figure 2.8: Meshes used. The first run using conservative grid spacing (a), and the second run using coarse grid spacing (b). Non-uniform spacing shows the GLL points along with the global elements.

2.6.3 Boundary Conditions

The boundary conditions that were applied to the computation channel domain are as follows:

- $v = 0$ at the top and bottom walls
- periodic boundary conditions on both the x-direction and z-direction faces

A periodic boundary condition in a computation domain is essentially replicating the domain an infinite number of times in order to avoid needing to set an inlet and outlet to the domain and the conditions needed with them. Periodic boundary conditions are convenient to use due to the ease of implementation while avoiding the need be concerned with the spatial development of the flow in a finite domain. Instead, periodic boundary conditions essentially create an environment where user is solely concerned with the time development of the flow.

2.6.4 Implementation of Wall Model

The wall model is implemented through a logical switch addefor a Finite Element, Chebyshev collocation, and Legendre spectral element solutions d to the Nek5000 source code. The switch is set to true when the user wants to use the wall model. The first step was assigning a Dirichlet boundary condition at the wall for the y-velocity, v. This is done simply by assigning $v = 0$ as a boundary condition in the *user* file and Nek5000 will assign the condition on any element face that user has designated a wall. The second step was to set a Robin boundary condition on the stress at the wall. Nek5000 uses three Helmholtz solves in order calculate the x, y,

and z velocities in which the weak form of the Naiver-Stokes equations are used.

$$\left(\nu\nabla^2 r, q\right)_\Omega = -\int_\Omega \nu\nabla r \cdot \nabla q \partial V + \int_{\partial\Omega} \nu\nabla r \cdot \hat{n} q \partial S \tag{2.62}$$

Using the divergence theorem, a boundary integral is obtained. In the boundary integral, $\nabla r \cdot \hat{n}$ is of concern for setting a boundary condition. The model takes the form of,

$$\mu\frac{\partial u}{\partial y}|_0 = \tau_{w,bc} \equiv \frac{u(y^+ = \delta)}{\langle u(y^+ = \delta)\rangle_{exp}} \langle\tau_w\rangle_{exp} \tag{2.63}$$

While the value of $u(y^+ = \delta)$ could simply be used as is, this value is not easily known. The value of y^+ is dynamic, depending on the friction velocity. Because of this, the value could easily end up somewhere in an element that is not directly on a GLL point. If this was the case, the value would need to be interpolated, which is an expensive operation to perform. Instead, the value of δ is assumed constant and the value of velocity is approximated using a first order Taylor expansion taken about the point at the wall.

$$\mu\frac{du}{dy} \approx \frac{u + \delta\frac{du}{dy}|_0}{\langle u\rangle_{exp}} \langle\tau_w\rangle_{exp} \tag{2.64}$$

where δ is the distance y^+, in wall units, away from the wall where the velocity value is taken to correlate with the stress at the wall. The new form of the boundary condition resembles a Robin boundary condition. The new boundary condition is

rearranged to resemble the Robin form and the values for a, b, and c are determined.

$$au + b\frac{\partial u}{\partial y} = c \tag{2.65}$$

$$\left(\mu - \delta\frac{\langle\tau_w\rangle_{exp}}{\langle u\rangle_{exp}}\right)\frac{du}{dy}|_0 - u\frac{\langle\tau_w\rangle_{exp}}{\langle u\rangle_{exp}} = 0 \tag{2.66}$$

$$\frac{\langle\tau_w\rangle_{exp}}{\langle u\rangle_{exp}} = a \tag{2.67}$$

$$\left(\mu - \delta\frac{\langle\tau_w\rangle_{exp}}{\langle u\rangle_{exp}}\right) = b \tag{2.68}$$

$$0 = c \tag{2.69}$$

The condition is solved for $\frac{\partial u}{\partial y}$ and this is the what is used in the weak formed Navier-Stokes equation to set the stress boundary condition. All the experimental values are taken from the DNS data in the work done by Hoyas and Jiménez [13]. These values are used in the weak formed Helmholtz solve as terms added at the boundaries.

3 RESULTS AND DISCUSSION

The test case of a turbulent channel was run using 8th order spectral elements on 128 processors at Texas A&M's supercomputer, EOS. The first run used approximately 5,000 CPU hours accumulating just over 82 seconds of real time flow data and the second run used approximately 600 CPU hours accumulating 800 seconds of real time flow data.. In these 82 seconds and 800 seconds respectively, the flow began as a laminar flow and transitioned to turbulent flow.

The main objective of this study was to test the speed and accuracy of a wall model for an LES of a turbulent channel when combined with a massively parallel, spectral element code, and validate the results against a DNS. An important detail to remember in the present study is that the boundary conditions are set using experimental values of u_τ and $U(y^+ = 100)$ and are not allowed to fluctuate. Typically, the values of u_τ as well as y^+ will fluctuate depending on the flow behavior. In a second iteration of this wall model, these values will be determined and set by the flow itself, allowing for fluctuations and more accurate results. With that said, the present wall modeled LES performed well in the first run, exhibiting similar turbulent and overall flow characteristics to the work of Hoyas and Jiménez. For an idea of the overall flow behavior, Figures 3.1 and 3.2 show the instantaneous and time-averaged velocity field and profile respectively at an arbitrary timestep. The turbulent behavior of the instantaneous velocity field is clearly seen while the time-averaged field shows a much smoother profile with a thinner boundary layer and sharper gradients, as expected. Figures 3.3-3.5 show the mean velocity profiles of the DNS, Wall Modeled LES, and a comparison of the two respectively.

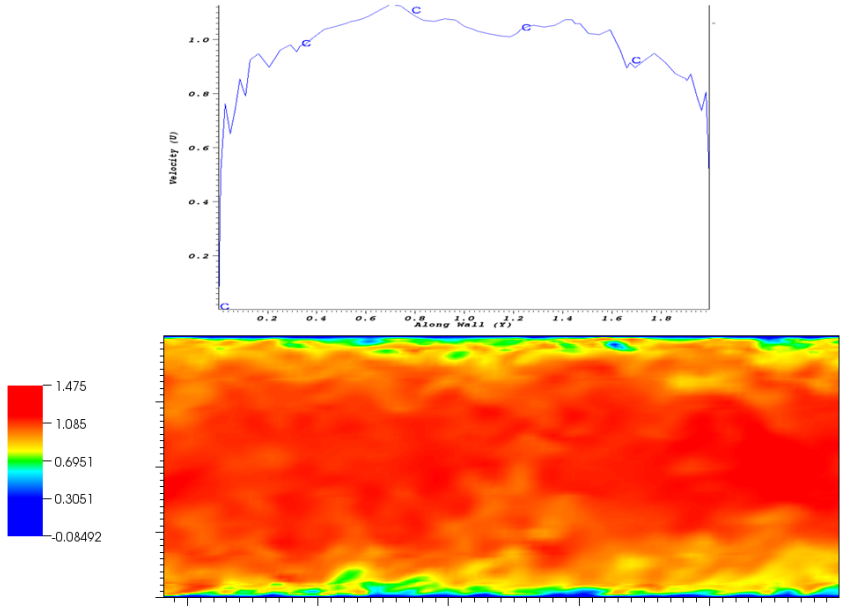

Figure 3.1: Instantaneous Velocity Profile. A Z-plane slice of the instantaneous velocity field along with a lineout of the velocity profile

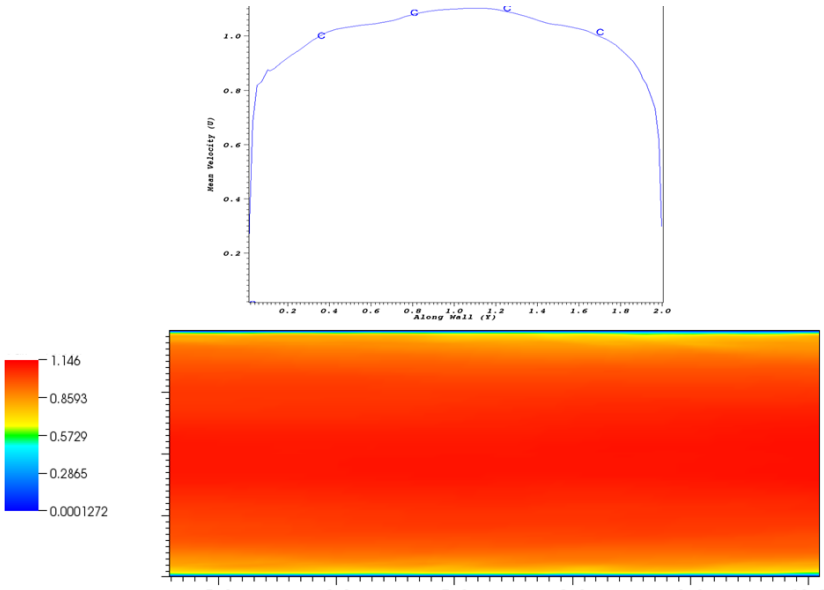

Figure 3.2: Time-Averaged Velocity Profile. A Z-plane slice of the time-averaged velocity field along with a lineout of the velocity profile

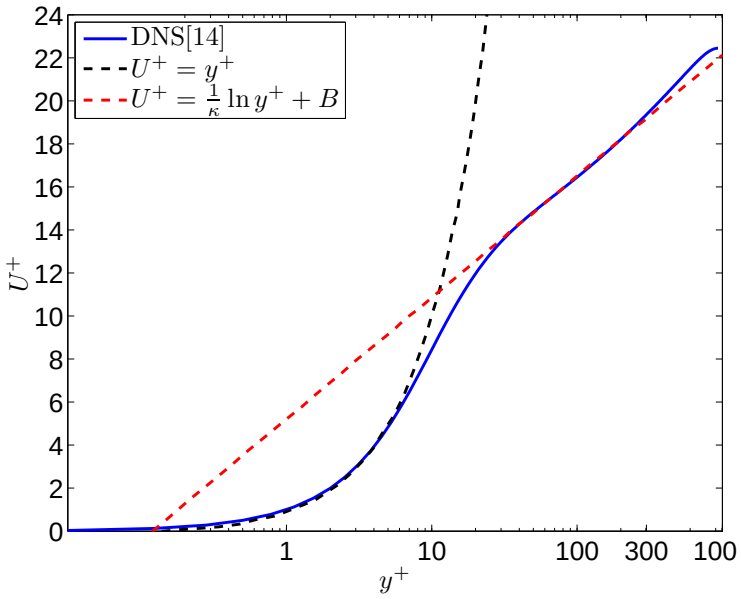

Figure 3.3: DNS Log-Law profile. Mean Velocity profile of DNS data in $Re_\tau = 950$ turbulent channel flow

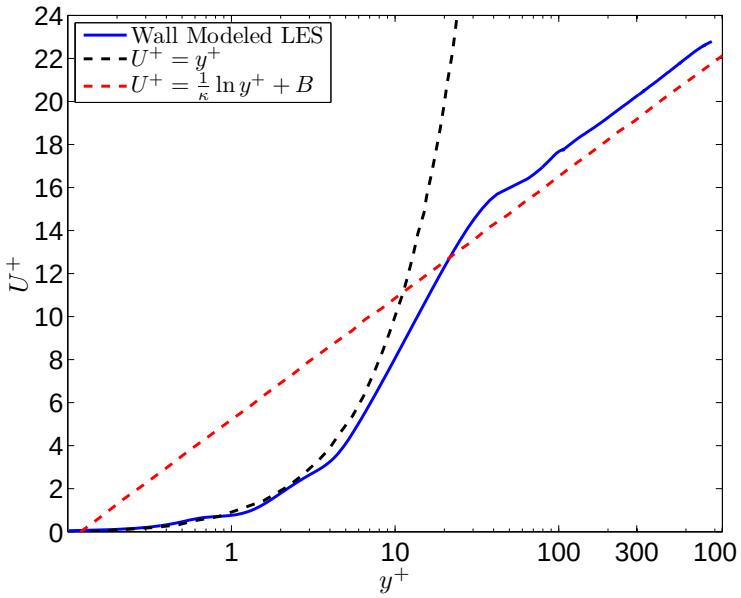

Figure 3.4: Wall modeled LES Log-Law profile. Mean Velocity profile of Wall Modeled LES data in $Re_\tau = 950$ turbulent channel flow

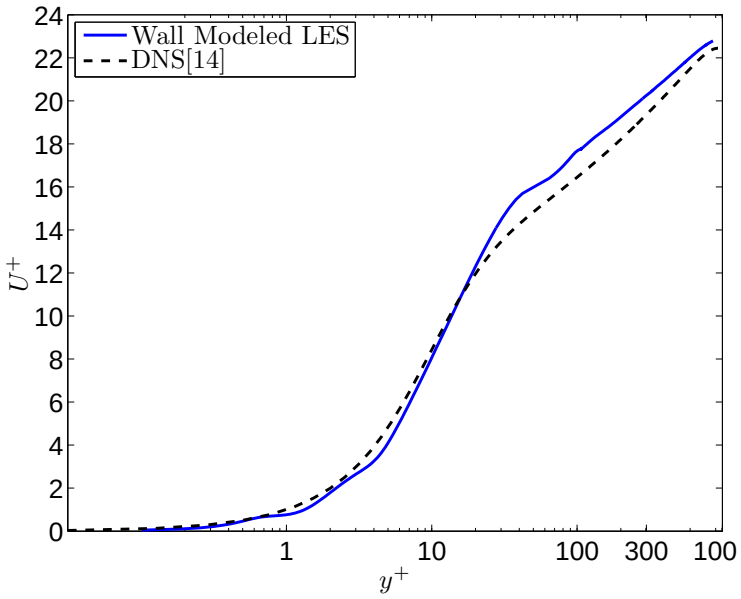

Figure 3.5: Comparision of wall Modeled LES and DNS Log-Law profile

In the viscous sub-layer, $0 < y^+ < 5$, the wall model deviates slightly from the $u^+ = y^+$ and in the log-law region, the model overshoots the DNS data curve but still retains the correct trend. This behavior of the mean velocity in the outer layer is seen in the implementation of the Dynamic Smargorinski model work done by Germano [9]. The higher values of mean velocity in the outer layer, where the Reynolds stress is primarily responsible for dissipating energy in the flow, is evidence of too little energy dissipation and an under-prediction of the Reynolds stress and eddy viscosity in the buffer region. A low value for the eddy viscosity could be due to an improper filter width calculated by the Dynamic Smagorinski model used. Figures 3.6-3.8 show the root-mean-square turbulence intensities $\sqrt{u'^2}$, $\sqrt{v'^2}$, and $\sqrt{w'^2}$. The turbulence intensities clearly peak in the near-wall region, as expected, and follow the same trends as the DNS data in the outer layer. The model slightly under predicted the turbulence intensities in the majority of the flow field, however, u_{rms} and w_{rms} were over predicted in the near-wall region around $y^+ = 50$. This is believed

to a be result of the values supplied as boundary conditions for the wall shear stress at the wall. Since u_τ, ν, and $U(y^+ = 100)$ were fixed, experimental values instead of dynamic, time-dependent terms calculated from the flow at each time step, the turbulence intensities were over predicted in the near-wall region. Figure 3.9 shows the Reynolds Shear Stress term $\langle u'v' \rangle$. Similar to the turbulence intensities, the Reynolds Shear stress was also slightly under-predicted and fluctuations are seen in the near-wall region. The under-prediction of the the Reynolds stress curve in the buffer region could be the cause of the velocity values being over-predicted. The velocity approaches the actual values further in the outer layer due to the model predicting higher Reynolds stresses than the DNS data. Figure 3.10 shows the Reynolds Stress terms plotted as a function of y^+. The trend and magnitude of the specific components matches what was expected as seen in Pope [24] for turbulent channel flow.

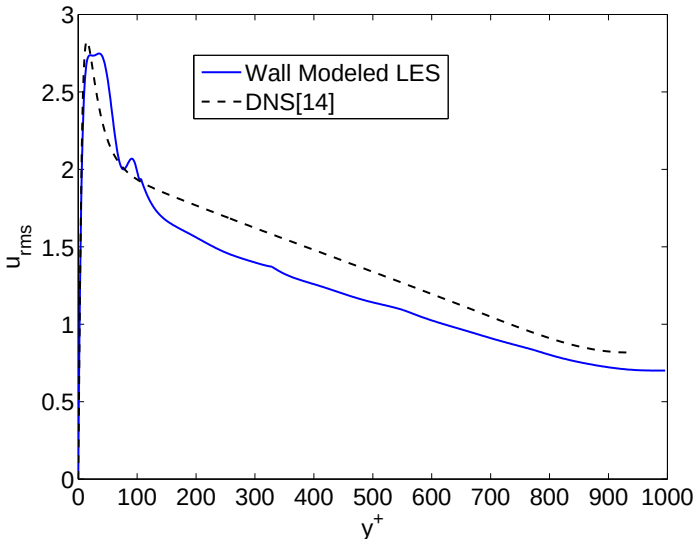

Figure 3.6: u_{rms} vs. y^+. Plane-averaged rms turbulence intensities $\sqrt{u'^2}$ normalized by friction velocity in $Re_\tau = 950$ turbulent channel flow, in wall units, y^+

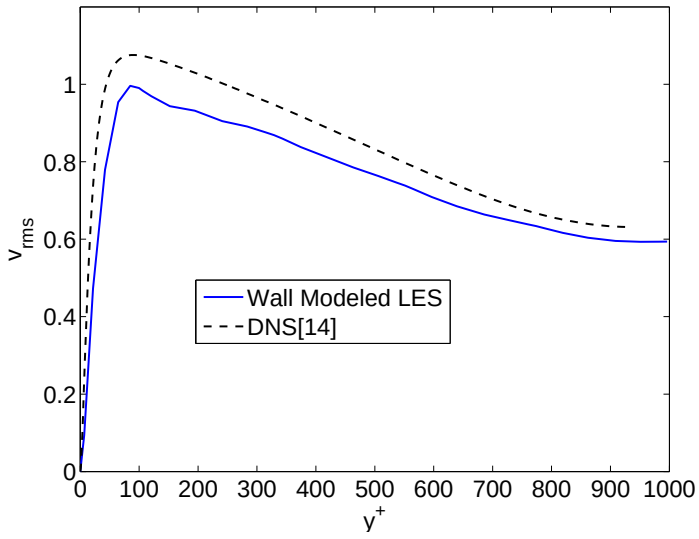

Figure 3.7: v_{rms} vs. y^+. Plane-averaged rms turbulence intensities $\sqrt{v'^2}$ normalized by friction velocity in $Re_\tau = 950$ turbulent channel flow, in wall units, y^+

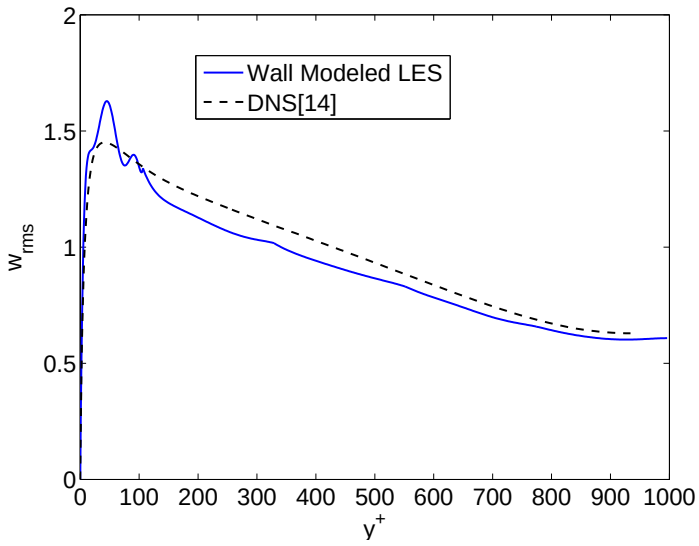

Figure 3.8: w_{rms} vs. y^+. Plane-averaged rms turbulence intensities $\sqrt{w'^2}$ normalized by friction velocity in $Re_\tau = 950$ turbulent channel flow, in wall units, y^+

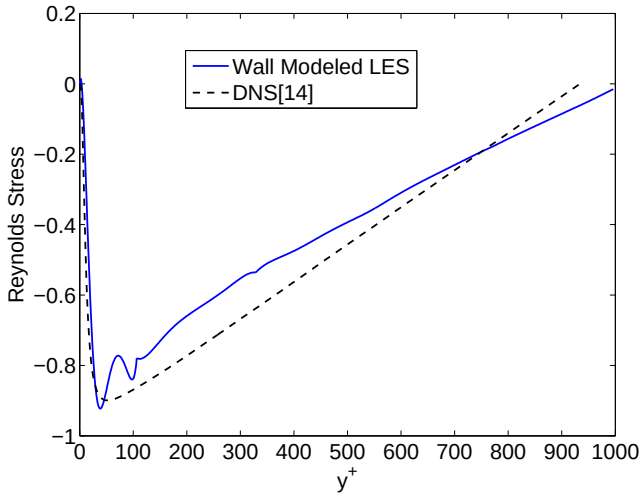

Figure 3.9: Reynolds Shear Stress vs. y^+. Plane-averaged Reynolds Shear Stress $u'v'$ normalized by friction velocity in $Re_\tau = 950$ turbulent channel flow, in wall units, y^+

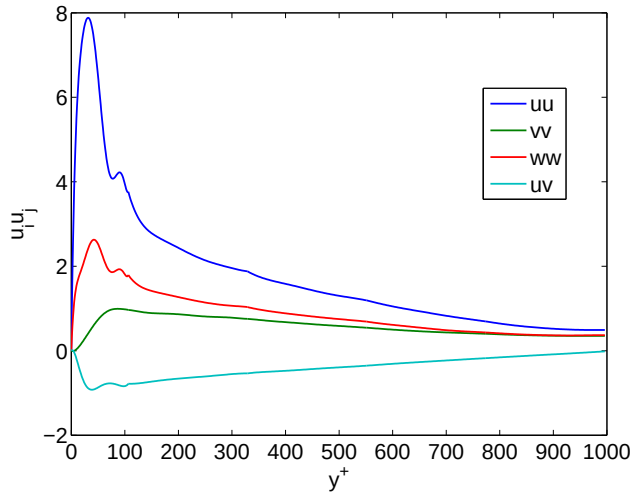

Figure 3.10: $u_i'u_j'$ vs. y^+. Plane-averaged Reynolds Stresses normalized by friction velocity in $Re_\tau = 950$ turbulent channel flow, in wall units, y^+

The second run with a much coarser mesh did not fare as well as the first run.

The mean velocity was vastly over-predicted in the outer layer. The velocity profile eventually reached a logarithmic-like shape, however, the mean velocity value itself was very high compared to the DNS data, as shown in Figures 3.11 and 3.12. Because of this, the buffer layer extended far past it's typical value. u_{rms} and w_{rms} decayed very rapidly due to the very high values compared to the DNS data. The Reynolds Stresses matched the proper profiles as the DNS data, however, the values were incorrectly predicted, shown in Figures 3.13-3.17. The Reynolds shear stress was under-predicted and decayed slightly faster than it should have and v_{rms} appears under-resolved due to the lack of clear maximum and weak decay rate, as shown in Figure 3.14. The velocity in the outer layer never approaches the actual values because the Reynolds stress continues to diverge from the DNS predicted values, as shown in Figure 3.16. These results clearly show a grid dependence is still necessary in order to capture the necessary turbulent data.

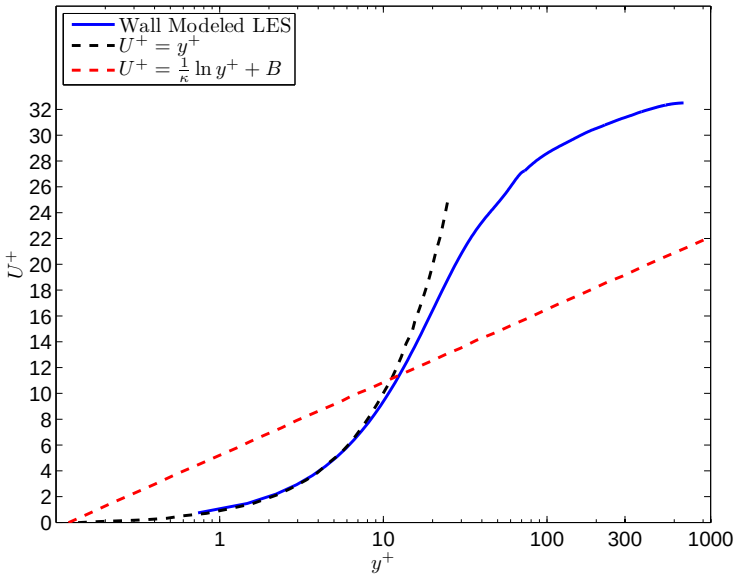

Figure 3.11: Coarse wall modeled LES Log-Law profile. Mean Velocity profile of Wall Modeled LES data in $Re_\tau = 950$ turbulent channel flow for large grid spacing

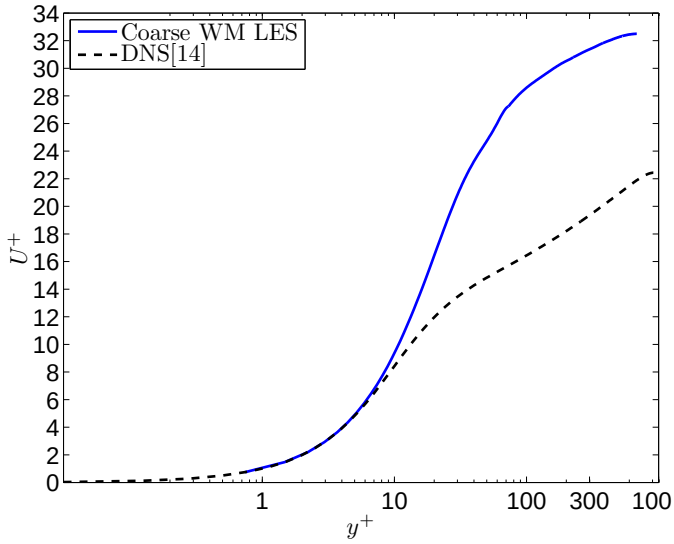

Figure 3.12: Comparision of coarse wall modeled LES and DNS Log-Law profile

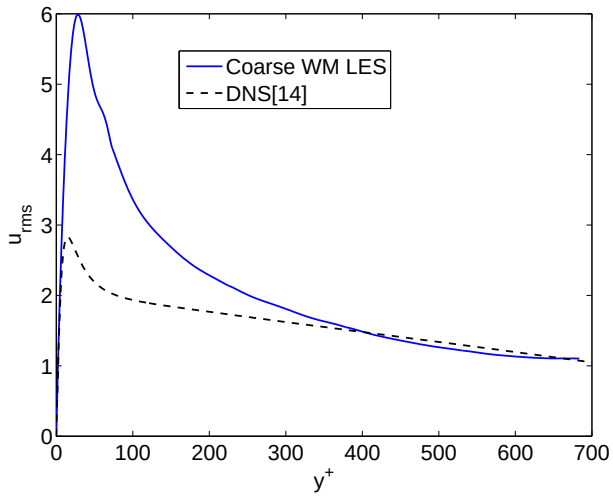

Figure 3.13: u_{rms} vs. y^+ for coarse mesh. Plane-averaged rms turbulence intensities $\sqrt{u'^2}$ normalized by friction velocity in $Re_\tau = 950$ turbulent channel flow, in wall units, y^+, for large grid spacing

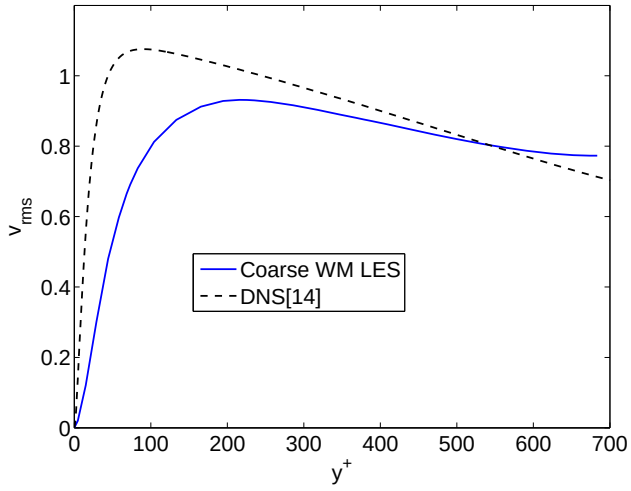

Figure 3.14: v_{rms} vs. y^+ for coarse mesh. Plane-averaged rms turbulence intensities $\sqrt{v'^2}$ normalized by friction velocity in $Re_\tau = 950$ turbulent channel flow, in wall units, y^+, for large grid spacing

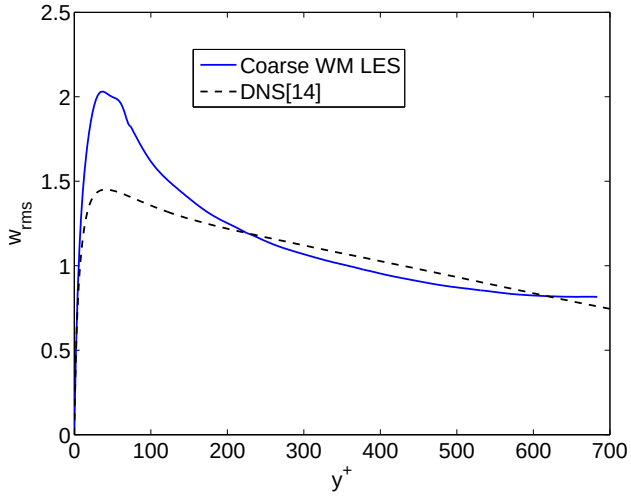

Figure 3.15: w_{rms} vs. y^+ for coarse mesh. Plane-averaged rms turbulence intensities $\sqrt{w'^2}$ normalized by friction velocity in $Re_\tau = 950$ turbulent channel flow, in wall units, y^+, for large grid spacing

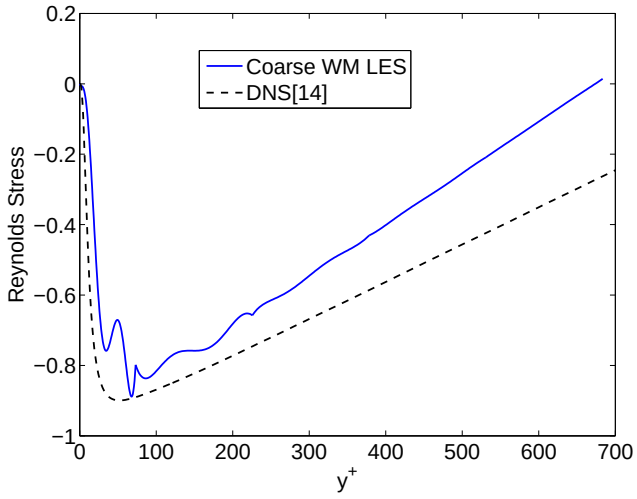

Figure 3.16: Reynolds Shear Stress vs. y^+ for coarse mesh. Plane-averaged Reynolds Shear Stress $u'v'$ normalized by friction velocity in $Re_\tau = 950$ turbulent channel flow, in wall units, y^+, for large grid spacing

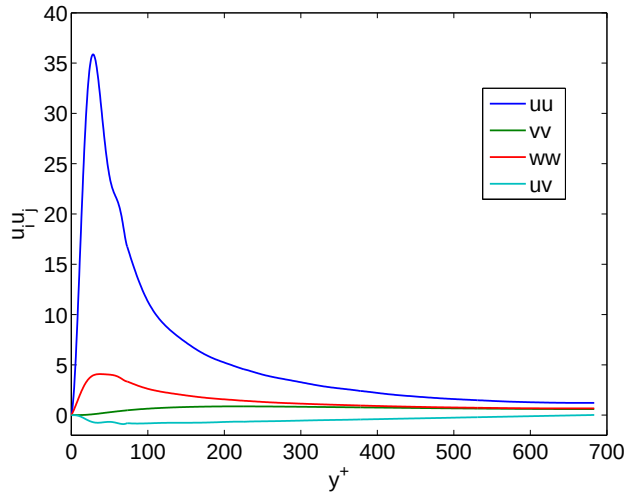

Figure 3.17: $u_i'u_j'$ vs. y^+ for coarse mesh. Plane-averaged Reynolds Stresses normalized by friction velocity in $Re_\tau = 950$ turbulent channel flow, in wall units, y^+, for large grid spacing

4 CONCLUSION AND FUTURE WORK

The use of a wall model in the massively-parallel, spectral element code, Nek5000 proved to be extremely beneficial in the LES of a turbulent channel. While the second run showed that, even with a wall model, an LES needs grid requirements in order to capture pertinent turbulent data, the first run proved that the original LES mesh requirements could be relaxed while still providing accurate results. The wall modeled LES reduced the required number of elements by over 70% from 112,986 elements down to 28,140 elements and only used about 5,000 hours to transition from laminar to turbulent flow as well as reach a statistically steady state. The error in the results for u_{rms}, v_{rms}, w_{rms}, and u'v' that were introduced by the approximate boundary conditions were very acceptable, especially with the benefit of the element count and computational time reduction.

The advantage gained with this wall modeled LES shows promise toward using LES for design purposes in real engineering applications, however, there are still several steps that need to be taken before such uses can be considered. The first minor step, as mentioned previously, is modifying the present model to use real flow data from the simulation itself to supply the boundary conditions at the wall, as well as taking elongated structures into account as done by Piomelli [23]. This should both improve the accuracy further and make the model more applicable to other types of flows. The second minor step would be to modify the model to allow for complex geometries. This step should be able to be accomplished through identifying wall normal components instead of simply an XYZ Cartesian system. The next major step would be incorporating a method to deal with secondary flows. When phenomena such as re-circulation and re-laminarization are involved, simple

approximate boundary conditions may not be enough to fully characterize these flows. Addressing these minor and major steps will further assist in the use of LES as a major engineering design tool in many industries.

REFERENCES

[1] Jeffrey S Baggett. On the feasibility of merging les with rans for the near-wall region of attached turbulent flows. *Annual Research Briefs*, pages 267–277, 1998.

[2] JS Baggett, F Nicoud, B Mohammadi, T Bewley, J Gullbrand, and O Botella. Suboptimal control based wall models for les including transpiration velocity. In *Proc. 2000 Summer Program*, pages 331–342, 2000.

[3] Elias Balaras, Carlo Benocci, and Ugo Piomelli. Two-layer approximate boundary conditions for large-eddy simulations. *AIAA Journal*, 34(6), 1996.

[4] W Cabot. Large-eddy simulations with wall models. *1995.*, pages 41–50, 1995.

[5] W Cabot. Near-wall models in large eddy simulations of flow behind a backward-facing step. *Annual Research Briefs 1996*, pages 199–210, 1996.

[6] P. A. Davidson and Mark Nelkin. Turbulence: An Introduction for Scientists and Engineers. *Physics Today*, 58, 2005.

[7] James W Deardorff. A numerical study of three-dimensional turbulent channel flow at large reynolds numbers. *Journal of Fluid Mechanics*, 41(2):453–480, 1970.

[8] M.O. Deville, P.F. Fischer, and E.H. Mund. *High-Order Methods for Incompressible Fluid Flow*. Cambridge University Press, New York, NY, 2002.

[9] Massimo Germano, Ugo Piomelli, Parviz Moin, and William H Cabot. A dynamic subgrid-scale eddy viscosity model. *Physics of Fluids A: Fluid Dynamics*, 3:1760, 1991.

[10] Richard J. Goldstein. *Fluid Mechanics Measurements*. Taylor and Francis, Philadelphia, PA, 2nd edition, 1996.

[11] Günther Grötzbach. Direct numerical and large eddy simulation of turbulent channel flows. In *Encyclopedia of Fluid Mechanics Volume 6*, pages 1337–1391, Houston, TX, 1987. Gulf Publishing Company.

[12] Melissa Green. Turbulent channel structures, December 2007. http://scienceasart.wordpress.com/.

[13] Sergio Hoyas and Javier Jiménez. Index of /channel/data, July 2006. http://torroja.dmt.upm.es/channels/data/statistics/Re950/profiles/Re950.prof.

[14] Sergio Hoyas and Javier Jiménez. Scaling of the velocity fluctuations in turbulent channels up to re[sub tau] = 2003. *Physics of Fluids*, 18(1):011702, 2006.

[15] Sergio Hoyas and Javier Jiménez. Reynolds number effects on the reynolds-stress budgets in turbulent channels. *Physics of Fluids*, 20(10):101511, 2008. http://link.aip.org/link/?PHF/20/101511/1.

[16] Javier Jimenez and Sergio Hoyas. Turbulent fluctuations above the buffer layer of wall-bounded flows. Cambridge Univ Press, 2008.

[17] PJ Mason and NS Callen. On the magnitude of the subgrid-scale eddy coefficient in large-eddy simulations of turbulent channel flow. *Journal of Fluid Mechanics*, 162(1):439–462, 1986.

[18] Chin-Hoh Moeng. A large-eddy-simulation model for the study of planetary boundary-layer turbulence. *Journal of the Atmospheric Sciences*, 41(13):2052–2062, 1984.

[19] F Nicoud, JS Baggett, P Moin, and W Cabot. Large eddy simulation wall-modeling based on suboptimal control theory and linear stochastic estimation. *Physics of Fluids*, 13:2968, 2001.

[20] Paolo Orlandi. *Fluid Flow Phenomena A Numerical Toolkit*. Kluwer Academic Publishers, Norwell, MA, 2000.

[21] James W. Lottes Paul F. Fischer and Stefan G. Kerkemeier. nek5000 Web page, 2008. http://nek5000.mcs.anl.gov.

[22] U. Piomelli. Large-eddy and direct simulation of turbulent flows. In *Introduction to the Modelling of Turbulence*, Rhode Saint Gene'se, Belgium, 2000. von Karman Institute for Fluid Dynamics.

[23] Ugo Piomelli, Joel Ferziger, Parviz Moin, and John Kim. New approximate boundary conditions for large eddy simulations of wall-bounded flows. *Physics of Fluids*, 1:1061–1068, 1989.

[24] Stephen B. Pope. *Turbulent Flows*. Cambridge University Press, New York, NY, 2000.

[25] S. Rajagopalan and R. A. Antonia. Some properties of the large structure in a fully developed turbulent duct flow. *Physics of Fluids*, 22(4):614–622, 1979.

[26] G Schrauf. Status and perspectives of laminar flow. *Aeronautical Journal*, 109(1102):639–644, 2005.

[27] U. Schumann. Subgrid scale model for finite difference simulations of turbulent flows in plane channels and annuli. *Journal of Computational Physics*, 18(4):376–404, 1975.

[28] H. Werner and H. Wengle. Large-eddy simulation of turbulent flow over and around a cube in a plane channel. In *Turbulent Shear Flows 8*, pages 155–168–, Munich, Germany, 1993. Springer.

[29] Xiaohua Wu and Kyle D Squires. Prediction of the three-dimensional turbulent boundary layer over a swept bump. *AIAA Journal*, 36(4):505–514, 1998.